Jurnal

by Rakhmat Kurniawan R

Submission date: 10-Jan-2023 07:27AM (UTC+0700)
Submission ID: 2119350258
File name: JURNAL_Q2.pdf (3.15M)
Word count: 6361
Character count: 32838

A Micromechanical Data-Driven Machine-Learning Approach for Microstructural Characterization of Solder Balls in Electronic Packages Subjected to Thermomechanical Fatigue

R. Rakhmat Kurniawan[1] · Biju Theruvil Sayed[2] · Arif Sari[3] · Jorge Paucar Luna[4] · A. K. Kareem[5] · Naseer Ali Hussien[6]

Abstract
A combination of nanoindentation mapping and machine-earning (ML) modeling has been used to characterize the micro-structural changes in SnPb solder balls exposed to thermal cycling. The model facilitated the microstructural evaluation of solder bumps through the prediction of microscale variations of Young's modulus in the joint zone. The outcomes revealed that the micromechanical data-driven ML model precisely classified the microstructural constituents, i.e., β-Sn and α-Pb, along with the grain boundary (GB) regions. However, some deviations were observed in GB recognition, when the elastic modulus gradient was not sharp enough. The predictive results also revealed that the increase in number of thermal cycles led to stiffening and grain coarsening of α-Pb, while the β-Sn matrix mainly remained stable. Moreover, it was found that the thermal cycling intensified structural heterogeneity in the solder and sharpened the elastic modulus variations at the GB regions. In summary, the outcomes of this study demonstrate the prediction possibility of microstructural features in SnPb solder balls with a predefined thermal cycle numbers, and unfolded the relationship between morphological characteristics and microscale mechanical properties.

Keywords Solder balls · thermomechanical fatigue · thermal cycling · machine learning · nanoindentation

R. Rakhmat Kurniawan is co-corresponding author.

✉ R. Rakhmat Kurniawan
rakhmat.kr@uinsu.ac.id

✉ Arif Sari
arifsari@gau.edu.tr

[1] Department of Computer Science, Universitas Islam Negeri Sumatera Utara Medan, Medan, Indonesia

[2] Department of Computer Science, Dhofar University, Salalah, Oman

[3] Department of Management Information Systems, Girne American University, Kyrenia, North Cyprus, Turkey

[4] Departamento Académico de la Facultad de Ingenieria Industrial, Universidad Nacional Mayor de San Marcos, Lima, Perú

[5] Biomedical Engineering Department, Al-Mustaqbal University College, Babylon, Iraq

[6] Information and Communication Technology Research Group, Scientific Research Center, Al-Ayen University, Thi-Qar, Iraq

Introduction

Solder joints are incontrovertible components in electronic packages, electrically and mechanically connecting the substrate and other components.[1–3] Considering their brittleness behavior, solder joints have been identified as the weakest parts, leading to de-functioning of electronic systems if they fail under thermomechanical loadings.[4–6] This event is more critical in solder ball grid arrays with miniaturized dimensions. Hence, great efforts have recently been made to evaluate the microstructural features and mechanical response of solder balls subjected to thermal cyclic loadings.[7–10] To give some examples, Marbut et al.[11] proposed a novel methodology for characterizing the mechanical shear stresses induced from thermal expansions. They successfully established a meaningful relationship between the plastic work accumulation of solders and the fatigue life in a generic device by using a method on the basis of controlled force application and spring deflection. Depiver et al.[12,13] simulated the inelastic plasticity evolution of solder ball joints with different alloying compositions under accelerated thermal cycling, and found that the thermomechanical fatigue

properties of lead-free SnAgCu solders were comparable to eutectic $Sn_{63}Pb_{37}$ solder; however, Ghaleeh et al.[14] reported that the SnAgCu solder balls are less sensitive to changes of temperature. Romdhane et al.[15] revealed that the orientation of tin grains in solder balls altered the stress states in the joint zone, so that it significantly affected the reliability of ball grid array components. They also used electron backscattered diffraction analysis to determine the role of microstructural features on the fatigue life, finding that crack initiation was accompanied by the propagation of recrystallized β-Sn grains in the solder balls, especially in their high strain zones.[16] Xu et al.[17] established a multiscale approach with a combination of individual solder modeling at the crystal microscale and board-scale modeling at the continuum macroscale, which was able to precisely characterize the fatigue features of solder balls through the microstructure-sensitive parameters. Khatibi et al.[18] reported that PbSnAg solder joints subjected to cyclic loading aging treatments generally failed through the delamination of intermetallic compounds at the interfaces. In another study, Sakane et al.[19] established a numerical model to correlate the creep fatigue lifetime of SnPb solders with the rate of grain boundary (GB) sliding in the microstructure. An investigation into the SnPb solder joints also showed that the crack propagation along the intermetallic compounds is the main failure mechanism under vibration loading, while the cracking in the bulk of the solder plays a crucial role in thermal cycling damage.[20] Li et al.[21] demonstrated that a small addition of Ag into SnPb solder impeded the excessive growth of Pb-rich grains under thermal cycling. Tian et al.[22] reported that thermal stresses induced by extreme thermal shock leads to intermetallic growth at the interfaces of SnPb solder joints. Long et al.[23] proposed a model for estimating the fatigue lifetime of SnPb solder joints on the application of coupled thermal-electrical loadings. It was found that the simultaneous effects of heat sink temperature and current density significantly decreased the fatigue life of solder joints.

Machine learning (ML) has recently become interesting for studying the fatigue properties of solder joints in electronic systems.[24,25] However, the proposed ML models have mainly focused on the physical parameters of solder joints for estimating the fatigue lifetime under different states.[26–29] To be specific, the models collected the input parameters, such as geometry features, thermal load specifications, and physical properties of solder interconnections, and established a ML-based algorithm to predict the fatigue lifetime as the target. Hence, until now there has been no published work characterizing the fatigue microstructure of solder joints through ML-based approaches. To implement a ML model for microstructural characterization, it is crucial to have a huge dataset with specific details about the microstructural characteristics of solder joints. Nanoindentation mapping is an efficient procedure, not only providing a huge number of indentation data from the material but it can also trace the microstructural features in a whole picture.[30–32] Using this method, it is possible to detect the microscale mechanical response of a material, which is an indicator of microstructural evolution under an external excitation, such as thermomechanical loading. Inspired by such techniques, for the first time we try to establish a ML model based on nanoindentation-mapping data, which enables microstructure characterization of solder bumps subjected to a wide range of thermomechanical cyclic loading. The outcomes of this work throw light on the design of solder interconnections with the highest fatigue lifetimes.

Experimental

In recent years, due to environmental issues, the application of SnPb solders has been restricted in the electronics industry. However, SnPb usage still continues in rare cases. Moreover, the investigation of SnPb solders has facilitated the identification of creep fatigue damage in Sn-based solder joints. Hence, as explained in the "Introduction", there are numerous recent published works studying SnPb solder failure under external loadings. In this study, chip-scale packaged ball grid arrays (BGA) comprised of 196 SnPb solder bumps were applied for materials characterization. The diameter of the solder balls was on average 550 μm, while the package dimensions were 15 mm × 15 mm × 1.4 mm. Figure 1a depicts the structure of the BGA chip of interest including the main dimensions in mm. The die and the attach thicknesses are 0.3 mm and 0.1 mm, respectively. Solder paste and subsequent underfill were used for the interconnections. A proper stencil with a round aperture fitted to the BGA chip was used for printing the solder pastes. Then, a typical reflow profile was applied to solder the BGA package to the printed circuit board. A daisy chain verification was performed to evaluate the integrity of the solder interconnections. A convection reflow oven with multiple heating and cooling zones was employed for the reflow process. Accordingly, solder interconnections were formed via the melting of the solder paste. The BGA packages were exposed to a thermal cycling process with a temperature range of 273–403 K, dwell time of 5 min, and heating/cooling rates of 30 K/min (see Fig. 1). The as-prepared sample along with the samples subjected to 3000 and 6000 cycles were considered for the following experiments. It should be noted that the selection of 6000 cycles as the maximum loading is associated with the crack initiation at the interface of the solder bumps. A magnified image of crack initiation is shown in Fig. 1. After the thermomechanical process, the microstructures of the samples were characterized through nanoindentation mapping equipped with a nano-positioning module. It should be noted that the solder bump at the

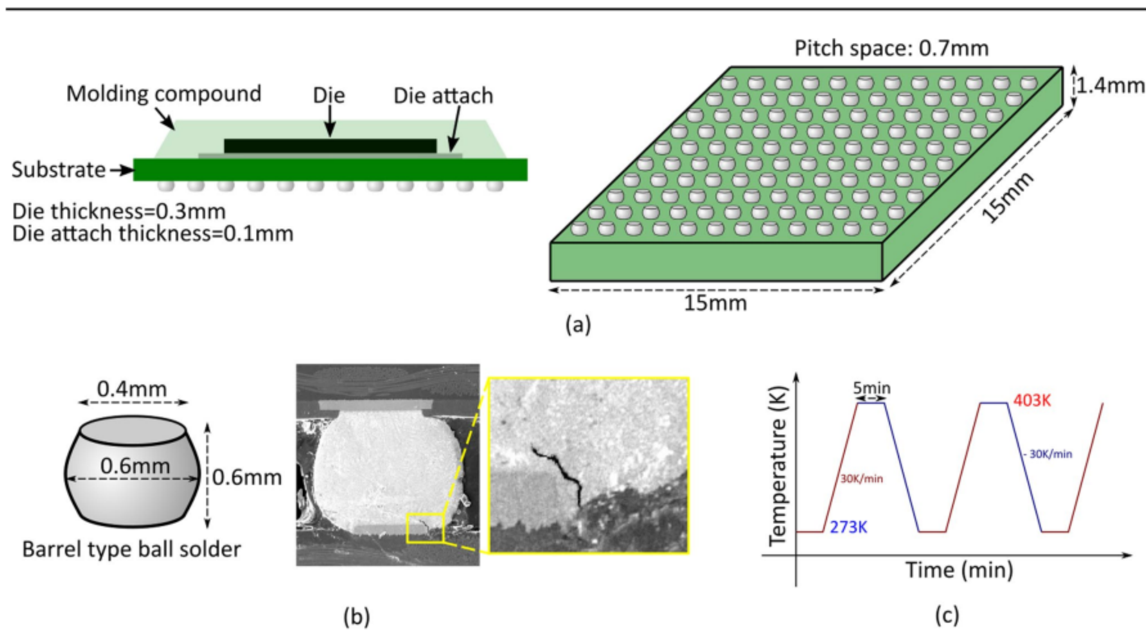

Fig. 1 (a) Schematic of ball grid arrays, (b) solder bump with detailed dimensional data (magnified image shows crack initiation in the solder bump load cycled 6000 times), (c) thermal cycling features.

corner site of the assembly, as the most vulnerable part,[33] was considered for this experiment. Nanoindentation testing (NanoTest Vantage) was conducted on a surface at the center of solder bumps with windows of 100 μm × 100 μm by a diamond Berkovich tip. Before calculating the elastic modulus of surface through the Oliver and Pharr technique,[34] the correction of load-frame compliance and area function calibration on fused silica were carried out. It should be noted that the indenting load was low enough to create a slight indent spacing/indent depth ratio. Selecting a proper maximum load prevents high noise-to-signal data acquisition and the low resolution of the indenting maps. In this work, a maximum load of 2mN, which creates ~ 35–50 nm depth, and 0.50-μm interval spacing were considered for capturing the mechanical properties of the solder balls at microscale. An image-based method was also applied to improve the resolution of the indentation maps.

A Prediction Model for Microstructure Characterization

In this paper, a new approach has been developed for estimating the microstructural characteristics of solder balls under different thermal cycles. As previously mentioned, the microstructure of a solder ball is directly affected by its inherent characteristics and the number of thermal cycles to which it is exposed. The aims of this method are to predict and to evaluate the main features of thermally loaded solder balls using three loaded and unloaded sets of data via ML and a mixture of experts (MoE). Three solder balls under 0, 3000, and 6000 thermal cycles were used for training the proposed prediction model. Accordingly, there exist three independent datasets to establish the model. Each dataset includes 250,000 data arrays. Figure 2 demonstrates the global structure of the proposed method for estimating the microstructure of the solder ball under any arbitrary number of thermal cycles. This method enables us to predict the behavior of the solder bump under thermal loading. As shown in the figure, each of the thermal loaded solder ball (i.e., 0, 3000, and 6000 thermal cycles) constitutes a separate and detached regression machine-learning box which can predict the mechanical features of the loaded solder bump. Then, all the estimated Young's moduli extracted from each ML box have been multiplied into gate parameters (determined by the gating network) in order to allocate weight factors to each prediction. Finally, the results were summed and the Young's modulus of an arbitrary pixel was calculated. In the following, the detail of ML and MoE will be discussed.

Machine-Learning Prediction Tool

Machine learning has gained attention in recent years owing to its flexibility in capturing and mapping any arbitrary inputs to the outputs (targets) via a training process using specified datasets.[35–37] The ML tool is a

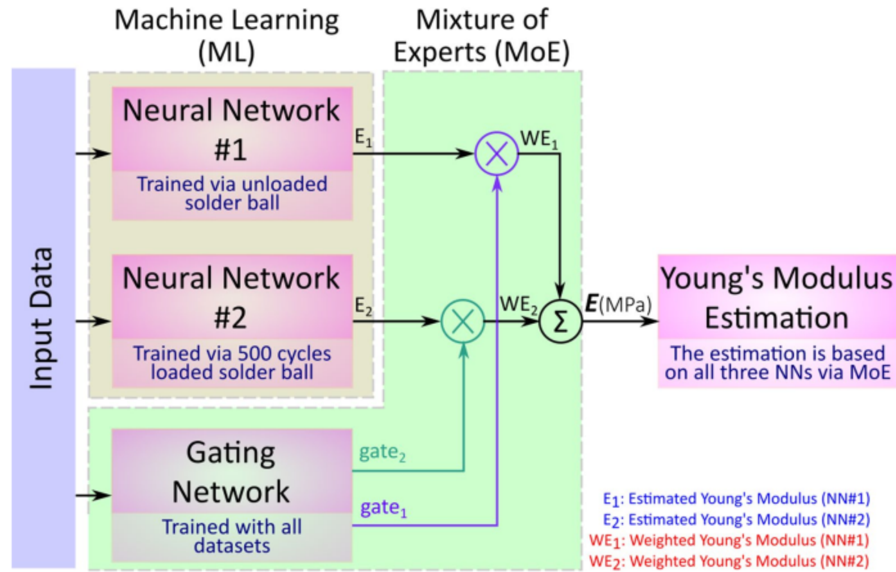

Fig. 2 Schematic of the proposed approach for structure characterization of the solder balls under thermal loading; ML constituted from two neural networks which are combined using MoE and the gate network.

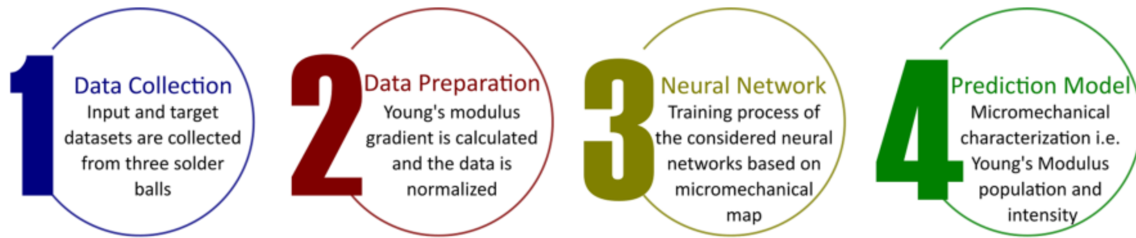

Fig. 3 Schematic of sequential stages of the machine-learning algorithm; this procedure is used for both neural networks.

generic estimator for connecting the input data to the output through minimizing the error of its predictions and the specified datasets. Figure 3 illustrates the sequential stages of the machine-learning algorithm. As shown, it consists of four different stages, namely, data collection, data preparation, neural network, prediction model. In the first stage, background datasets were collected for training of the neural network. The micromechanical map of the solder ball, i.e., the Young's modulus of each pixel, and the number of thermal cycles were considered as the input and target datasets. Two ML boxes were defined to correlate solder ball #1 (0 thermal cycle) to solder ball #2 (3000 thermal cycles) and solder ball #2 to solder ball #3 (6000 thermal cycles). The Young's modulus of each pixel of the micromechanical map and its gradient, as well as the number of thermal cycles of the solder balls #1 and #2, have been considered as the input datasets, and the Young's modulus of its corresponding pixel in solder balls #2 and #3 as the target datasets, respectively, for the first and second ML boxes (see Fig. 2). The input dataset size is $11 \times 250{,}000$, which means that there exist 11 contributory factors for each prediction; the target is $1 \times 250{,}000$. In the second stage, namely data preparation, two important manipulations were carried out. First, for an arbitrary pixel, the Young's modulus gradients with its neighbors were calculated, as shown in Fig. 4a. These values, as well as the number of thermal cycles of the input solder ball and the target ball, construct the input datasets ($11 \times 250{,}000$). The output (target) is the Young's modulus of the target solder ball and needs no further preparation. In the literature, it has been proven that, by normalizing the datasets in the lower range, the prediction performance may be boosted.[25] In this regard, we consider a normalization formulating for all the training datasets as:

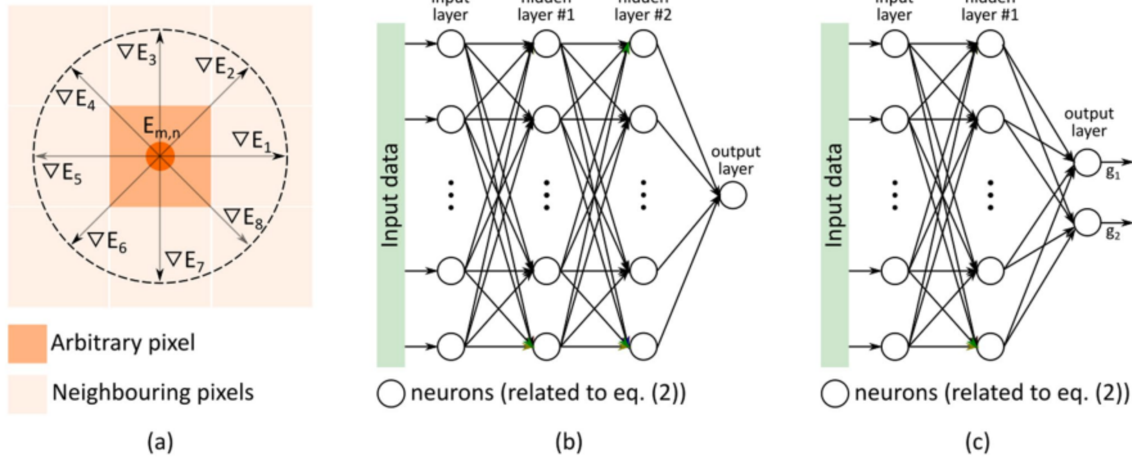

Fig. 4 Detailed information of the critical parts of the proposed prediction model: (a) definition of each pixel's Young's modulus and its neighboring pixels, (b) structure of the neural networks, and (c) structure of the gating network with two gating parameters for sharing the neural network contribution on the final Young's modulus prediction.

$$x_{new} = b_l + \frac{(b_u - b_l)(x - \min(x))}{\max(x) - \min(x)} \tag{1}$$

where x_{new} is the normalized value of its actual value (x), max(.) and min(.) are the maximum and minimum of the x vector, and b_l and b_u are the lower and upper bounds of the defined range, namely $(b_l\ b_u)$. The bounds may have any arbitrary values with the constraint of $b_u > b_l$. However, previous studies demonstrated that b_u and b_l in the order of 0.8–1.0 and 0.0–0.2, respectively, can be a wise choice and will maximize the performance of the global prediction model.[38,39] The third stage belongs to the core of the machine-learning prediction model, i.e., the neural network training process. In this step, a neural network with a predefined structure has to be trained in order to minimize the root mean square error (RMSE) and to maximize the determination factor (r) based on the prepared input and target datasets. The considered neural network has one input, and two intermediate hidden and one output layers. Thus, there exist a total of four layers with the number of neurons of [11 35 35 1]. Figure 4b depicts the considered neural network in this study. Each neuron consists of two individual formulations, i.e., the previous layer weighting and activation function. The output of a neuron can be formulated as:

$$y_i^{\ell} = f\left(\sum_{j=1}^{N_{\ell-1}} \omega_{ij}^{l} y_i^{\ell-1} + b_i\right) i = 1, \ldots, N_{\ell} \tag{2}$$

where i and l denote the neuron number and the layer number, respectively. Therefore, y^l_i is the output of the ith neuron number in the lth layer number, b_i is the bias value which can take any real values, and ω^l_{ij} is the weighting factor which correlated the output of previous letter to the current neuron. The main goal of the training process is to calculate these weighting factors in order to optimize the performance of the neural network. Function f(.) is the activation function and is in charge of integrating the neuron outputs. Several functions may be used, such as sigmoid, rectified linear unit, and binary step.[40] The sigmoid function has been employed in this training process as it facilitates smooth gradient convergence and is known as an appropriate normalization function. The sigmoid equation is defined as:

$$f(x) = \frac{1}{1 + e^{-x}} \tag{3}$$

The last stage of the machine-learning box is related to the final preparation of the desired output. As previously mentioned, the output of the ML is the Young's modulus of each pixel based on the associated pixel and its neighboring pixels of the three solder balls. Accordingly, one can easily find the Young's modulus population of any solder ball under the desired thermal cycles. As an example, based on NN_1, the E_1 of each pixel may be calculated with its associated pixel and its gradients of the solder ball #1, as well as the desired number of thermal cycles (i.e., 4500 cycles). In addition to predicting the Young's modulus of each pixel, an interface between two different phases can be evaluated by considering the following equation for each pixel, provided that the following condition is held for three adjacent pixels:

$$\begin{cases} \frac{E_{m,n} - E_{m,n+1}}{E_{m,n}} > 0.2 \\ \frac{E_{m,n} - E_{m,n-1}}{E_{m,n}} > 0.2 \end{cases} \quad (4)$$

where $E_{\mathrm{m,n}}$ is any arbitrary considered pixel in the predicted map. Using this expression, it enables the estimation of the number of interface pixels and the investigation of the micromechanical behavior of the solder ball under thermal loading.

Application of Mixture of Experts (MoE)

MoE has recently been used in several artificial intelligence structures.[41,42] The main goal of MoE is to combine two or more functions (outputs) with each other to obtain a desired output. In this paper, we have two separate neural networks (Fig. 2), and need to mix the outputs of these two ML boxes by attaining the weight of each output based on the input data. In this regard, a gating network has to be trained, based on the input and target datasets, in order to characterize the share of each neural network in the final Young's modulus prediction. The structure of the gating network is shown in Fig. 4b. Since there are experts, the output layer of the gating network has two neurons, i.e., g_1 and g_2. The input layer of the gating network is compatible with the other experts' input data. Only one hidden layer with 20 neurons is considered. The gating network is trained in order to minimize RMSE error of the final Young's modulus prediction ($\boldsymbol{E} = g_1E_1 + g_2E_2$) using a likelihood optimization method with respect to the target while holding the following condition for all the input datasets:

$$g_1 + g_2 = 1 \quad (5)$$

Once the gating network becomes trained and processed, one can use the gating parameters (g_1 and g_2) to determine the share of each expert (NN1 or NN2).

Results and Discussion

Predictive Efficiency in Microstructural Characterization

Figure 5 represents the microstructure of the solder bumps in the as-prepared sample along with the nanoindentation map from the center of the solder interconnection for all the samples. The SEM image shows that the solder bump mainly comprises a eutectic microstructure with α-Pb (bright color) and β-Sn (dark color) constituents. The nanoindentation maps cover 100 × 100 μm^2, demonstrating the distribution of the elastic modulus on the surface. The similarity between the SEM image and the indenting maps shows that the indent spacing is sufficient to capture the microstructural variations by the nanoindentations. It also confirms that the indentation mapping is capable of monitoring the abrupt change of the elastic modulus among the microstructural constituents. Considering the micromechanical maps, our ML model was implemented for characterizing and predicting the microstructural features in different numbers of thermal cycles. As can be seen, the increase in thermal cycle numbers leads to a change in the elastic response of the solder, which will be discussed later.

As a fundamental step, it is essential to justify the performance of the ML in predicting and characterizing the predefined targets. As depicted in Sect. "Machine Learning Prediction Tool"- "Introduction", there are three main outputs, i.e., α-Pb and β-Sn constituents and GB regions, which are defined from the solder microstructure on the basis of their elastic modulus values. The receiver operating characteristic curves, as indicators for predictive classification of predefined regions, are plotted in Fig. 6a. Based on the results, the ML model exhibits an exceptional performance in classifying the outputs with highly precise true-positive rate. The accuracy rates of 98.7%, 97.6%, and 93.6% for respectively discerning the Pb-based constituent (α), Sn-based matrix (β), and GB targets validate the predictive model as an outstanding classifier. Applying the regression technique, the deviation of outcomes from the input data has been calculated and presented in Fig. 6b, c ,and d. As can be observed, an immense part of the data for all three outputs is distributed near the line of 0% deviation, implying the model efficiency for predicting the elastic modulus and its variations in each predefined region of the solder microstructure. However, it can be seen that the data distribution is more sporadic in the E_{GB} output so that it lies between -3.2% to + 3.1% deviation. This deviation is more obvious in low E_{GB} values, meaning that the model is more efficient in identifying sharper gradients at the α/β interfaces. Excluding this result, there is no other meaningful correlation between the elastic modulus values and the data deviation.

Figure 7 represents the variations of E_α, E_β and E_{GB} as a function of the thermal cycle numbers. As mentioned, there exist few outliers (less than 0.1%) contradicting the bulk of the outcomes. Accordingly, they are omitted from the predicted outputs to confirm the cohesion in the results. Considering Fig. 7, each parameter shows an individual trend under the evolution of the thermal cycle numbers, which originate from their microstructural features. It can be seen that the increase in thermal cycles leads to a moderate increment of E_α from 13.7–14.4 GPa to 14.8–19.1 GPa, demonstrating signs of hardening in the lead-based constituent. On the other hand, the E_β value shows a slight increase from 38.8–39.3 GPa to 38.9–40.1 GPa in the range of 0–4000 thermal cycles, and then a saturated state appears in the variation of

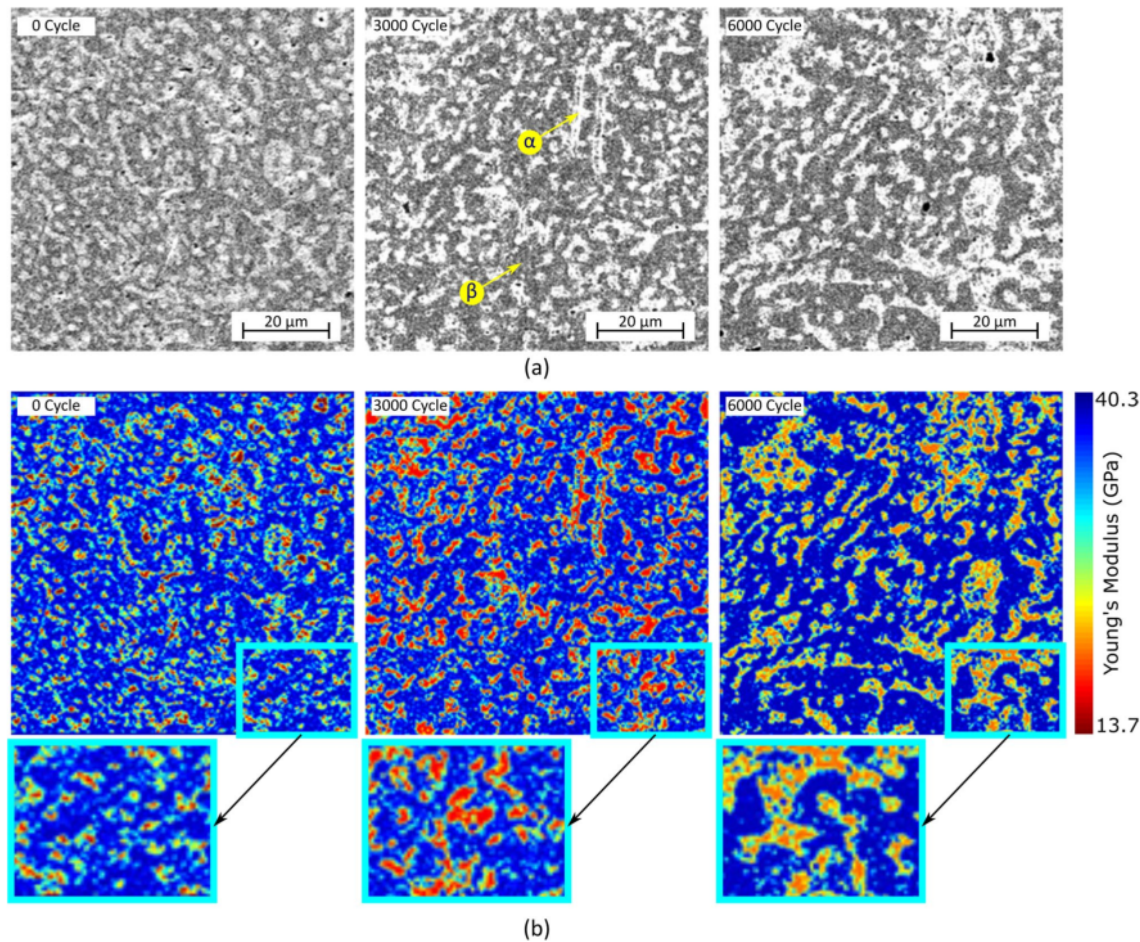

Fig. 5 (a) SEM micrographs from the center of solder bumps exposed to thermal cycling, and (b) their corresponding nanoindentation maps (a magnified region of the indentation map is presented for detailed observation).

the elastic modulus. For the third parameter (E_{GB}), the trend exhibits a stochastic evolution in the 0–4000 thermal cycles, and then a sharp rise is detected. Figure 8 illustrates the variations of N_α, N_β , and N_{GB} as a function of the thermal cycle numbers. The parameter N is an indicator of the number of regions with specific elastic modulus values. The results indicate that the increase in thermal cycle is accompanied by the N_α increment in the microstructure, while there exists a very slight decreasing trend in the N_β values. Moreover, N_{GB} shows a decreasing trend under thermal cycling, which is opposite to the N_α evolution. Considering the data given in Figs. 7 and 8, it is feasible to characterize the microstructural evolution under the thermal cycling. At a first glance, it can be seen that the E_α and N_α values show growing trends under thermal cycling, compatible with the hardening and grain coarsening in the lead-based constituent, respectively. It is suggested that the thermal cycling provides the activation energy for significant atomic interdiffusion in the system, which leads to solubility of the tin into the α constituent (< 2 at%) and the subsequent hardening effect. One should note that the α grain coarsening, manifested by the increase in N_α , follows static and dynamic processes.[43–45] Exposure to the peak temperature is correlated to the static mechanism, while the grain coarsening upon the induced strain of thermal cycling is associated with the dynamic mechanism.[46] Considering the β constituent, it is found that the E_β and N_β mainly exhibit neutral trends under thermal cycling, implying that the Sn-based matrix solely has the minimal influence on the microstructural degradation under thermomechanical fatigue. On the other hand, at high cycle numbers, the E_{GB} and

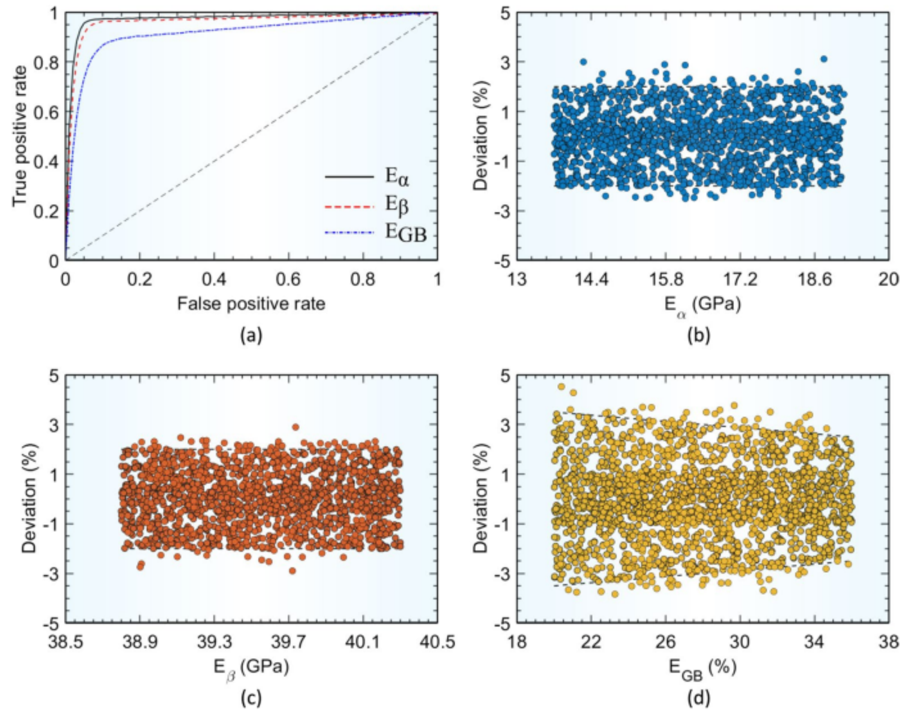

Fig. 6 (a) The receiver operating characteristic curves for the targets, and the deviation degree of predicted outputs from the measured inputs for (b) E_α, (c) E_β, and (d) E_{GB}.

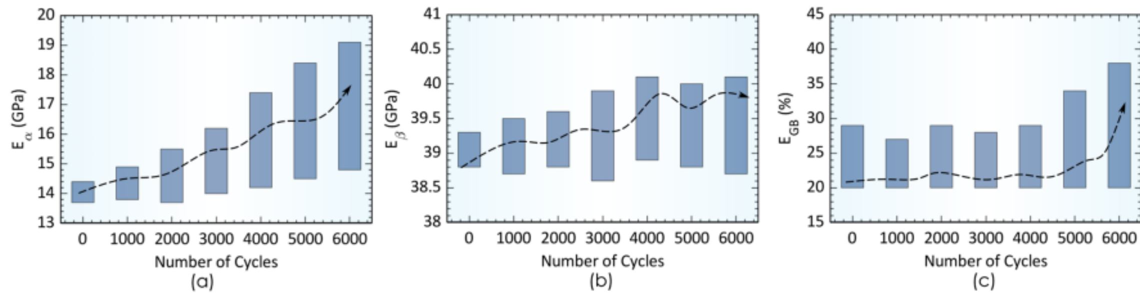

Fig. 7 Predictive outcomes of elastic modulus variations for (a) α, (b) β, (c) GB.

N_{GB} values show sharp alterations with increasing and decreasing trends, respectively. The enhancement of the E_{GB} value means that the gradient mechanical features of the α/β interface become intense, leading to stress concentration at the interfaces and phase separation in the microstructure.[47,48] Moreover, the decline of N_{GB} indicates the restriction of the α/β interfacial regions, which is consistent with the grain coarsening of the α constituent under the thermal cycling.

A Case Study

In this section, the microstructural/mechanical features of solder bump exposed to 4500 thermal cycles are characterized in detail. It should be noted that the micromechanical data of this sample were not applied in the ML training process. Figure 9a represents the experimental and predicted Gaussian distributions of elastic modulus (*E*) in the microstructure. The results indicate a significant overlap

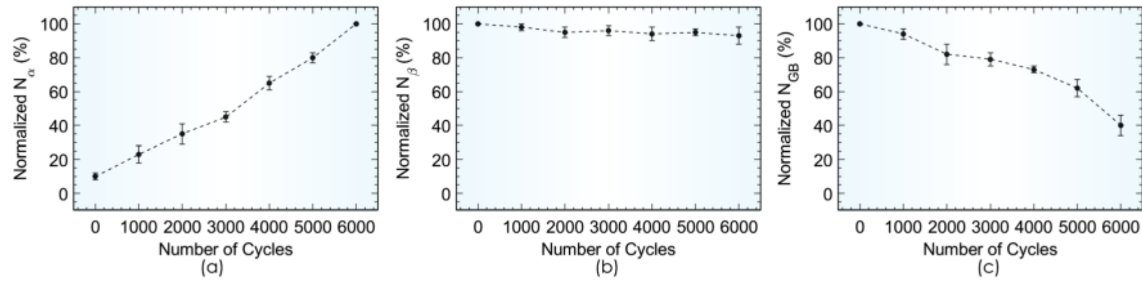

Fig. 8 Normalized population of predicted regions with determined elastic modulus for (a) α, (b) β, (c) GB.

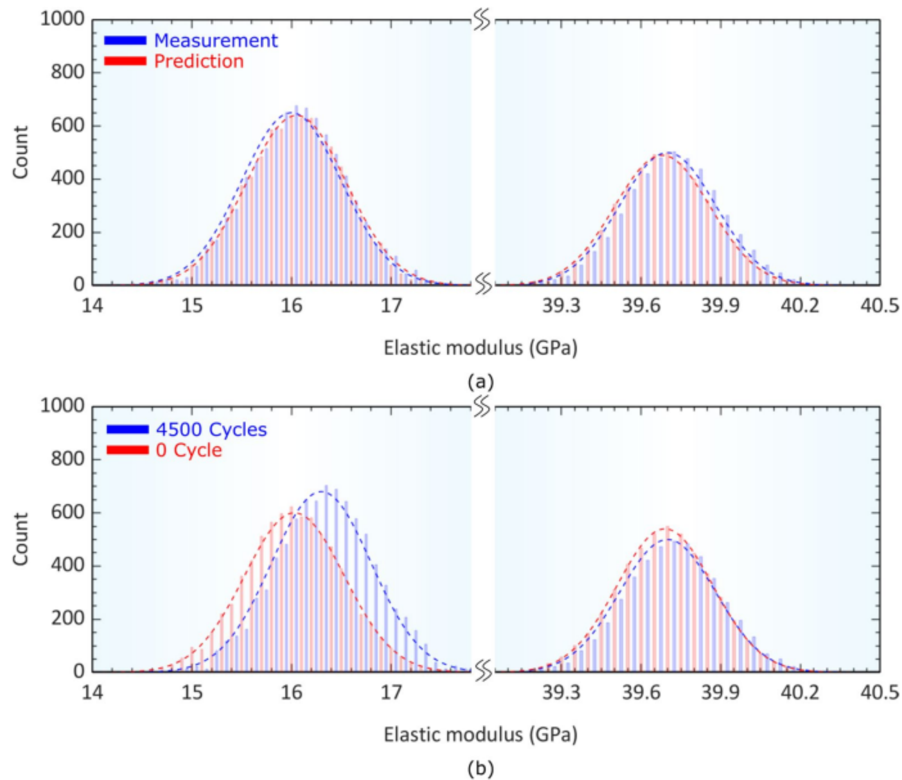

Fig. 9 Gaussian distribution of elastic modulus in (a) predicted and experimental outcomes of 4500-thermal-cycled samples, (b) as-prepared (0 cycle), and 4500-thermal-cycled samples.

between the plots, confirming the accuracy of ML outcomes for predicting the elastic modulus of the α and β constituents and their populations in the system. As also given in Fig. 9b, the peak position and peak intensities of the treated sample markedly change upon the thermal cycling so that the E_α peak shifts to the higher values, while the E_β peak mostly keeps its position. Moreover, the N_α population rises under the thermal cycling and the N_β remains stable. One should note that, since there exist fluctuations in the volume of the α/β interface under thermal cycling, it is not required to have the same ($N\alpha + N\beta$) values in the as-prepared and treated samples. Hence, it is concluded that the grain coarsening originates from the coalescence of the α constituent without affecting the volume of the β constituent in the microstructure. This process is due the fact that the solubility of Sn and Pb at room temperature is very low in the Sn–Pb binary system, hindering the extra atomic interdiffusion in the system.

To characterize the features of the α/β interface in the microstructure, a data deconvolution process was carried out to distinguish the hardness of the properties of the interfaces from the spatial map of the α–β bi-phase system. For this purpose, the k-means technique, as a data clustering algorithm, was applied to specify the interface volume. In this technique, k-means acts as an iterative refinement tool, in which the k cluster centers are initialized at random states and then the position of the cluster centers is displaced to new points, leading to minimization of the intra-cluster sum of squares of distances.[31] This iterative technique can efficiently detach the data into a prearranged number of clusters. The binned data can also be specified through the iterative running of the model with a wide range of cluster numbers and subsequent identification of an optimized state at the minimum error. After the data separation by the algorithm, the selected clusters with similar properties represent a predetermined position in the spatial map. Unlike the Gaussian deconvolution-based process, the K-means method keeps the spatial information, facilitating the mechanical evolution of local regions in the microstructure. Figure 10 illustrates the de-convoluted map of the elastic modulus at the α/β interfaces of the as-prepared and 4500-cycled samples, which are extracted from the nanoindentation mapping. At first glance, it can be seen that the E_{GB} value increases at the interfaces, showing the increase of mismatch in mechanical properties of the main constituents in the microstructure after thermal cycling. Moreover, the magnified map of data shows that grain coarsening clearly occurred in the solder, which is manifested by the average decrease of the N_{GB} value under the evolution of thermal cycling, as also confirmed in Sect. "Predictive Efficiency in Microstructural Characterization"-"Introduction". However, there are unrevealed features ignored in the data presented previously. For example, although the grain coarsening is accompanied by the decrease of N_{GB} value in the microstructure, one can see that the GB regions (interfacial areas) in the thermally-cycled sample are thinner, which shows sharper mechanical variations in this state. Moreover, the magnified images from the thermally-cycled sample clearly indicates that sharper E gradients of GBs are specifically located among the coarse grains created under the thermal cycling. In summary, it is concluded that thermal cycling intensifies structural heterogeneity in the solder and sharpens the mechanical variations at the interfaces. This event increases the stress concentration at the interfaces and expedites the nucleation of defects in the microstructure. In general, the results confirm that the thermomechanical process affects the solder microstructure under high cycling numbers and facilitates the damage evolution in the joint zone. As shown in Fig. 1, the crack initiation is one of the indicators of damage evolution which typically occurs at the interface of the solder and the substrate. There also exist other parameters, such as the rate of intermetallic formation in the solder/Cu pad zone defining the damage degree in the interconnection. It should be noted that it is hardly possible to capture the

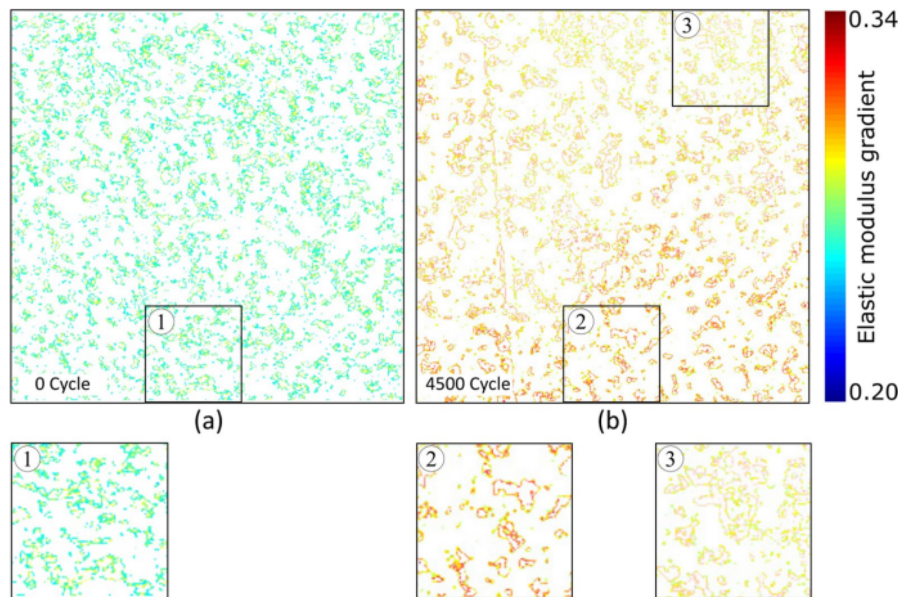

Fig. 10 De-convoluted data of GB regions for (a) as-prepared (0 cycle) sample and (b) 4500-thermal-cycled sample; the magnified image shows the details of GB features in the microstructure.

micromechanical variations near the crack region or to analyze the elastic modulus changes of SnPb microstructure and intermetallic zones at the interfaces simultaneously, due to some limitations in the nanoindentation process. Hence, this work tries to focus on the microstructural evolution of SnPb solder and to show how the Sn-based microstructure reacts to the regular thermal cycling occurring in an electronic system. The ML-based outcomes not only precisely predict the microstructural features of the solder material but also play a crucial role in characterizing the micromechanical features related to the damage evolution.

Conclusions

This work applied a combination of nanoindentation mapping and machine learning (ML) modeling to evaluate the microstructural variations in SnPb solder balls subjected to thermal cycling. The main outcomes of this investigation are as follows:

- The micromechanical data-driven ML model precisely classified the population of microstructural constituents, i.e., β-Sn and α-Pb, along with the GB regions in the joint zone. Some deviations were detected in the GB identification at a low elastic-modulus gradient.
- The rise in the number of thermal cycles led to stiffening and grain coarsening of the α-Pb constitute, while the β-Sn matrix mainly remained stable. It was also demonstrated that the thermal cycling intensified the elastic modulus variations in the GB regions. It is believed that the grain coarsening in the microstructure comes at the expense of GB reduction.
- Finally, the ML model is capable of predicting the microstructural features in SnPb solder balls in a wide range of thermal cycle numbers, facilitating the design of solder balls and reliability assessment in the electronic packages.

Conflict of interest The authors declare that they have no conflicts of interests.

References

1. N. Ismail, A. Atiqah, A. Jalar, M.A. Bakar, R.A.A. Rahim, A.G. Ismail, A.A. Hamzah, and L.K. Keng, *J. Manuf. Process.* 83, 68 (2022).
2. S. Zhou, Z. Lin, B. Qiu, H. Wang, J. Xiong, C. He, B. Zhou, Y. Pan, R. Huang, and Y. Bao, *Electronics* 11, 2556 (2022).
3. S. Zhang, H. Zhao, H. Xu, and X. Fu, *Microelectron. Reliab.* 120, 114094 (2021).
4. V. Samavatian, H. Iman-Eini, Y. Avenas, and M. Samavatian, *J. Electron. Mater.* 51, 5376 (2022).
5. J. Liang, Y. Zhong, S. Robertson, A. Liu, Z. Zhou, and C. Liu, *IEEE Trans Components Packag. Manuf. Technol.* 11, 2122 (2021).
6. Y. Maniar, A. Kabakchiev, M. Kuczynska, M. Bazrafshan, P. Binkele, and S. Schmauder, in *InInternational Electronic Packaging Technical Conference and Exhibition.* (American Society of Mechanical Engineers, 2021), p. V001T06A003.
7. R.M. Cibils, *IEEE Trans Compon Packag. Manuf. Technol.* 9, [illegible] (2019).
8. J.A. Depiver, S. Mallik, and E.H. Amalu, *Eng. Fail. Anal.* 125, 105447 (2021).
9. K.S. Tan, S.J. Oon, L.Y. Teng, T.Y. Tou, S.S. Yap, C.S. Lau, and Y.T. Chin, *Compos. Part B Eng.* 162, 461 (2019).
10. J. Han, F. Guo, and J.P. Liu, *J. Alloys Compd.* 698, 706 (2017).
11. C.J. Marbut, M. Montazeri, and D.R. Huitink, *IEEE Trans. Device Mater. Reliab.* 18, 412 (2018).
12. J.A. Depiver, S. Mallik, and E.H. Amalu, in *IEEE 8th Electron Syst. Technol. Conf.* 2020, 1–11 (2020).
13. J.A. Depiver, S. Mallik, and E.H. Amalu, *J. Electron. Mater.* 50, 263[illegible] (2021).
14. M. Ghaleeh, A. Baroutaji, and M. Al Qubeissi, *Eng. Fail. Anal.* 117, 104846 (2020).
15. E. Ben Romdhane, A. Guédon-Gracia, S. Pin, P. Roumanille, and H. Frémont, *Microelectron. Reliab.* 114, 113812 (2020).
16. E. Ben Romdhane, P. Roumanille, A. Guédon-Gracia, S. Pin, P. Nguyen, and H. Frémont, *Microelectron. Reliab.* 126, 114288 (2021).
17. Y. Xu, J. Xian, S. Stoyanov, C. Bailey, R.J. Coyle, C.M. Gourlay, and F.P.E. Dunne, *Int. J. Plast.* 155, 103308 (2022).
18. G. Khatibi, A. Betzwar Kotas, and M. Lederer, *Microelectron. Reliab.* 85, 1 (2018).
19. M. Sakane, T. Shiratsuchi, and Y. Tsukada, *Int. J. Fatigue* 146, 106132 (2021).
20. T. An, C. Fang, F. Qin, H. Li, T. Tang, and P. Chen, *Microelectron. Reliab.* 91, 213 (2018).
21. Q. Li, C.-F. Li, W. Zhang, W. Chen, and Z.-Q. Liu, *Microelectron. Reliab.* 99, 12 (2019).
22. R. Tian, C. Hang, Y. Tian, and J. Xu, *J. Mater. Process. Technol.* 268, 1 (2019).
23. X. Long, Y. Liu, Y. Yao, F. Jia, C. Zhou, Y. Fu, and Y. Wu, *AIP Adv.* 8, 85001 (2018).
24. V. Samavatian, M. Fotuhi-Firuzabad, M. Samavatian, P. Dehghanian, and F. Blaabjerg, *Sci. Rep.* 10, 14821 (2020).
25. V. Samavatian, M. Fotuhi-Firuzabad, M. Samavatian, P. Dehghanian, and F. Blaabjerg, *IEEE Trans. Compon. Packag. Manuf. Technol.* 12, 34[illegible] (2022).
26. Y. Sung and J. Robert, *Solder. Surf. Mt. Technol.* 32, 82 (2019).
27. A.A. Salameh, H. Hosseinalibeiki, and S. Sajjadifar, *Weld. World* 66, 2029 (2022).
28. A. Zippelius, A. Hanß, M. Schmid, J. Pérez-Velázquez, and G. Elger, *Microelectron. Reliab.* 129, 114461 (2022).
29. T.-C. Chen, F.J.I. Alazzawi, A.A. Salameh, and A. Al Ayub Ahmed, I. Pustokhina, A. Surendar, and A. Y. Oudah, *Mech. Adv. Mater. Struct.* 30(2), 373–381 (2021).
30. Y. Tong, H. Zhang, H. Huang, L. Yang, Y. Hu, X. Liang, M. [illegible], and J. Zhang, *Intermetallics* 135, 107209 (2021).
31. B. Vignesh, W.C. Oliver, G.S. Kumar, and P.S. Phani, *Mater. Des.* 181, 108084 (2019).
32. E.D. Hintsala, U. Hangen, and D.D. Stauffer, *JOM* 70, 494 (2018).
33. E.R. Arriola, A.T. Ubando, J.A. Gonzaga, and C.C. Lee, *Eng. Fail. Anal.* 144, 106986 (2022).
34. W.C. Oliver and G.M. Pharr, *MRS Bull.* 35, 897 (2010).

35. T.-C. Chen, R. Rajiman, M. Elveny, J.W.G. Guerrero, A.I. Lawal, N.K.A. Dwijendra, A. Surendar, S.D. Danshina, and Y. Zhu, *Arab. J. Sci. Eng.* 46, 12417 (2021).
36. K. Sabanci, *Measurement* 155, 107553 (2020).
37. M. Samavatian, R. Gholamipour, D.O. Bokov, W. Suksatan, V. Samavatian, and M. Mahmoodan, *J. Non. Cryst. Solids* 578, 121344 (2022).
38. A. Khan, S. Hayat, Y. Zhong, A. Arif, L. Zada, and M. Fang, *Alex. Eng. J.* 66, 957 (2023).
39. Y. Chen, N. Zhang, and J. Yang, *Neurocomputing* 515, 26 (2023).
40. L. Wan and Z. Liu, *Neurocomputing* 524, 1 (2023).
41. C. Park, P. Vincent, S. Chong, J. Park, Y.S. Cha and H. Cho, *Solid. State. Electron.* 199, 108500 (2023).
42. M. Vasić, A. Petrović, K. Wang, M. Nikolić, R. Singh, and S. Khurshid, *Neural Netw.* 151, 34 (2022).
43. W. Dreyer, and W.H. Müller, *Int. J. Solids Struct.* 37, 3841 (2000).
44. S.M. Xue, S. Zhou, X. Wang, X.-H. Zeng, and Z.-Q. Liu, in *2022 23rd International Conference on Electronic Packaging Technology* (IEEE, 2022), pp. 1–4.
45. G. Gan, D. Xia, X. Liu, C. Liu, H. Cheng, Z. Ming, H. Gao, D. Yang, and Y. Wu, Solder. *Surf. Mt. Technol.* 85–92 (2019).
46. P.T. Vianco, S.N. Burchett, M.K. Neilsen, J.A. Rejent, and D.R. Frear, *J. Electron. Mater.* 28, 1290 (1999).
47. W. Dreyer, and W.H. Müller, *Int. J. Solids Struct.* 38, 1433 (2001).
48. F. Wang, D. Li, S. Tian, Z. Zhang, J. Wang, and C. Yan, *Microelectron. Reliab.* 73, 106 (2017).

Publisher's Note Springer Nature remains neutral with regard to jurisdictional claims in published maps and institutional affiliations.

Springer Nature or its licensor (e.g. a society or other partner) holds exclusive rights to this article under a publishing agreement with the author(s) or other rightsholder(s); author self-archiving of the accepted manuscript version of this article is solely governed by the terms of such publishing agreement and applicable law.

Jurnal

ORIGINALITY REPORT

18%	10%	16%	2%
SIMILARITY INDEX	INTERNET SOURCES	PUBLICATIONS	STUDENT PAPERS

PRIMARY SOURCES

1	Tzu-Chia Chen. "Microstructural Characterization of Ti/Cu/Ti Diffusion Bonded System through a Micromechanical Data-Driven Neural Network Approach", Materials Today Communications, 2023 Publication	1%
2	www.gainhealth.org Internet Source	1%
3	Tzu-Chia Chen, Maria Jade Catalan Opulencia, Hasan Sh. Majdi, Ali Thaeer Hammid et al. "Estimation of Thermomechanical Fatigue Lifetime of Ball Grid Solder Joints in Electronic Devices Using a Machine Learning Approach", Journal of Electronic Materials, 2022 Publication	1%
4	Reza Reihanisaransari, Farshad Samadifam, Anas A. Salameh, Farzam Mohammadiazar, Nafiseh Amiri, Sittiporn Channumsin. "Reliability characterization of Solder Joints in Electronic systems through a Neural Network Aided Approach", IEEE Access, 2022 Publication	1%

5	B. Vignesh, W.C. Oliver, G. Siva Kumar, P. Sudharshan Phani. "Critical assessment of high speed nanoindentation mapping technique and data deconvolution on thermal barrier coatings", Materials & Design, 2019 Publication	1%
6	www.theses.fr Internet Source	1%
7	Gunawan Widjaja, Kirill Ershov, Supat Chupradit, Wanich Suksatan et al. "The effects of hydrogen doping on energy state of shear bands in a Zr-Based metallic glass", Vacuum, 2022 Publication	1%
8	Meiling Xin, Xiuqi Wang, Fenglian Sun. "Microstructure evolution, IMC growth, and microhardness of Cu, Ni, Ag-microalloyed Sn–5Sb/Cu solder joints under isothermal aging", Journal of Materials Science: Materials in Electronics, 2022 Publication	<1%
9	www.nature.com Internet Source	<1%
10	I. Dutta. "A constitutive model for creep of lead-free solders undergoing strain-enhanced microstructural coarsening: A first report", Journal of Electronic Materials, 2003	<1%

Publication

11	Yue Huang, Chun Lin. " An Evaluation Method for the Morphology of Large Format Detector Array ", Journal of Physics: Conference Series, 2020 Publication	<1%
12	ukmsarjana.ukm.my Internet Source	<1%
13	S h. Eshghi, M. Jafarpour, A. Darvizeh, S. N. Gorb, H. Rajabi. "A simple, high-resolution, non-destructive method for determining the spatial gradient of the elastic modulus of insect cuticle", Journal of The Royal Society Interface, 2018 Publication	<1%
14	case.asu.ru Internet Source	<1%
15	Chang-Chun Lee, Yu-Min Lin, Hou-Chun Liu, Ji-Yuan Syu, Yuan-Cheng Huang, Tao-Chih Chang. "Reliability evaluation of ultra thin 3D-IC package under the coupling load effects of the manufacturing process and temperature cycling test", Microelectronic Engineering, 2021 Publication	<1%
16	Yidian Shi, Ganglong Li, Cheng Peng, Wenhui Zhu, Hu He. "Microscale fracture toughness	<1%

degradation of notched solder microcantilevers under varied accelerated aging process", Journal of Materials Research and Technology, 2023

Publication

17	Yupeng Wang, Haibin Liu, Mingdong Bao, Wenhao Yang, Bing Zhou, Hung-Chun Wu. "Interfacial Reactions of Sn-3.0Ag-0.5Cu Solder with Sputter Cu-Ti Alloy Film UBM", Journal of Electronic Materials, 2021 Publication	<1 %
18	Zhijia Zhang, Baosen Zhang, Shuaishuai Zhu, Xuewei Tao, Haoliang Tian, Zhangzhong Wang. "Achieving enhanced wear resistance in CoCrNi medium-entropy alloy co-alloyed with multi-elements", Materials Letters, 2022 Publication	<1 %
19	aip.scitation.org Internet Source	<1 %
20	Majid Samavatian, Reza Gholamipour, Dmitry Olegovich Bokov, Wanich Suksatan, Vahid Samavatian, Morteza Mahmoodan. "Characterization of nanoscale structural heterogeneity in metallic glasses: A machine learning study", Journal of Non-Crystalline Solids, 2022 Publication	<1 %

21 Mathias Ekpu. "Investigating the Reliability of SnAgCu Solder Alloys at Elevated Temperatures in Microelectronic Applications", Journal of Electronic Materials, 2021 <1%
Publication

---

22 Mohammad Abdul Motalab, Md. Tusher Ahmed, Md. Omarsany Bappy. "Effect of thermal aging on electromigration failure of a flip-chip SnAgCu solder joint subjected to random vibration", AIP Publishing, 2021 <1%
Publication

---

23 Yan Wang, Jing Han, Fu Guo, Xiaoxing Ke. "Effects of Grain Orientation on the Electromigration of Cu-Reinforced Composite Solder Joints", Journal of Electronic Materials, 2017 <1%
Publication

---

24 utq.edu.iq <1%
Internet Source

---

25 parasitol.kr <1%
Internet Source

---

26 www.mdpi.com <1%
Internet Source

---

27 Canyu Liu, Han Jiang, Shuibao Liang, Allan Liu, Zhaoxia Zhou, Changqing Liu. "Bonding with Zn-based solders through self-propagating <1%

exothermic reaction to enable high-temperature electronics packaging", 2022 IEEE 24th Electronics Packaging Technology Conference (EPTC), 2022
Publication

---

28 E. Ben Romdhane, P. Roumanille, A. Guedon-Gracia, S. Pin, P. Nguyen, H. Fremont. "Evaluation of SAC solder joint thermomechanical fatigue in different types of components", 2022 23rd International Conference on Thermal, Mechanical and Multi-Physics Simulation and Experiments in Microelectronics and Microsystems (EuroSimE), 2022
Publication

<1 %

---

29 Jiaqiang Huang, Xudong Wang, Junyu Chen, Weichun Wei, Fengmei Liu, Binhao Qin, Haiyan Wang, Yupeng Zhang. "Growth mechanisms of intermetallic compounds and Bi-rich layer in ball grid array structure Cu/Sn-58Bi/Cu solder joints during solid–solid and liquid–solid electromigration", Journal of Materials Science: Materials in Electronics, 2022
Publication

<1 %

---

30 infor.seaninstitute.org
Internet Source

<1 %

---

31 www.hindawi.com
Internet Source

<1 %

32	David Kim, Maciej Marciniak. "Horizontal tail maneuver load predictions using backpropagation neural networks", 40th Structures, Structural Dynamics, and Materials Conference and Exhibit, 1999 Publication	<1%
33	Moujhuri Sau, Eric D. Hintsala, Youxing Chen, Douglas D. Stauffer et al. "High-Throughput Nanoindentation Mapping of Additively Manufactured T91 Steel", JOM, 2022 Publication	<1%
34	X. H. Guo. "Elastoplastic phase field model for microstructure evolution", Applied Physics Letters, 2005 Publication	<1%
35	dspace.lboro.ac.uk Internet Source	<1%
36	puma.ub.uni-stuttgart.de Internet Source	<1%
37	www.coursehero.com Internet Source	<1%
38	www.freepatentsonline.com Internet Source	<1%
39	Zhai Xinmeng, Chen Yue, Yuefeng Li, Zou Jun, Shi Mingming, Yang Bobo, Li Yang, Guo Chunfeng, Hu Rongrong, Cao Qinglou. "Effect of Solder Particle Size on the Mechanical and	<1%

Thermal Reliability of Au/Sn Ag Cu/Cu Solder Joints", ECS Journal of Solid State Science and Technology, 2021
Publication

40	alicia.concytec.gob.pe Internet Source	<1%
41	doaj.org Internet Source	<1%
42	www.osapublishing.org Internet Source	<1%
43	www.research-collection.ethz.ch Internet Source	<1%
44	www.thi.de Internet Source	<1%
45	Xiangqian Wang, Ningke Xu, Xiangrui Meng, Haoqian Chang. "Prediction of Gas Concentration Based on LSTM-LightGBM Variable Weight Combination Model", Energies, 2022 Publication	<1%
46	www.springerprofessional.de Internet Source	<1%
47	H. L. Lai, J. G. Duh. "Lead-free Sn-Ag and Sn-Ag-Bi solder powders prepared by mechanical alloying", Journal of Electronic Materials, 2003 Publication	<1%

48 spiral.imperial.ac.uk
Internet Source
<1 %

49 E. Ben Romdhane, P. Roumanille, A. Guédon-Gracia, S. Pin, P. Nguyen, H. Frémont. "From early microstructural evolution to intergranular crack propagation in SAC solders under thermomechanical fatigue", Microelectronics Reliability, 2021
Publication
<1 %

50 Vahid Samavatian, Hossein Iman-Eini, Yvan Avenas, Majid Samavatian. "Thermomechanical Fatigue Damage Model of a Solder Joint in Electronic Devices: An Interval Arithmetic Based Approach", Journal of Electronic Materials, 2022
Publication
<1 %

51 Adlil Aizat Ismail, Maria Abu Bakar, Abang Annuar Ehsan, Azman Jalar, Erwan Basiron, Fakhrozi Che Ani. "Cardinal and Ordinal Directions Approach in Investigating Arrayed Solder Joints Crack Propagation of Ball Grid Array Semiconductor Packages", IEEE Transactions on Components, Packaging and Manufacturing Technology, 2022
Publication
<1 %

52 Bhaskar Paul, Jugal Kishor, A. Karthik, Tammana S.R.C. Murthy, Saurav Sunil, K. Singh, Sanjib Majumdar. "The studies on the
<1 %

tribological performance, characterization and mechanical properties of W-2Ni-1Fe (wt%) alloy", International Journal of Refractory Metals and Hard Materials, 2021

Publication

53	Deekshith G. Kalali, Harita Seekala, P. Sudharshan Phani, K. Bhanu Sankara Rao, Koteswararao V. Rajulapati. "High speed nanoindentation aided correlative study between local mechanical properties and chemical segregation in equiatomic MoNb and MoNbTi alloys", Journal of Materials Research, 2023 Publication	<1%
54	Jianqing LI, Tzu-Chia Chen, Angelina Olegovna Zekiy. "Correlative study between elastic modulus and glass formation in ZrCuAl(X) amorphous system using a machine learning approach", Applied Physics A, 2021 Publication	<1%
55	Jiawen Cheng, Yong Xiao, Yun Shao, Guanghai Dong, Songlin Lyu, Wenjian Yu. "Machine-learning-driven Architectural Selection of Adders and Multipliers in Logic Synthesis", ACM Transactions on Design Automation of Electronic Systems, 2023 Publication	<1%

56	Ning Wang, Majid Samavatian, Vahid Samavatian, Haijun Sun. "Bayesian machine learning-aided approach bridges between dynamic elasticity and compressive strength in the cement-based mortars", Materials Today Communications, 2023 Publication	<1%
57	bingweb.binghamton.edu Internet Source	<1%
58	bjeps.alkafeel.edu.iq Internet Source	<1%
59	centaur.reading.ac.uk Internet Source	<1%
60	ir.library.osaka-u.ac.jp Internet Source	<1%
61	researchonline.ljmu.ac.uk Internet Source	<1%
62	www.science.gov Internet Source	<1%
63	Advances in Spectroscopy for Lasers and Sensing, 2006. Publication	<1%
64	Qihai Li, Wei Zhao, Wei Zhang, Weiwei Chen, Zhiquan Liu. "Research on thermal fatigue failure mechanism of BGA solder joints based	<1%

on microstructure evolution", International Journal of Fatigue, 2022
Publication

65 Anas A. Salameh, Hossein Hosseinalibeiki, Sami Sajjadifar. "Application of deep neural network in fatigue lifetime estimation of solder joint in electronic devices under vibration loading", Welding in the World, 2022 — <1%
Publication

66 Kento Uchida, Genki Sakata, Tetsushi Watari, Yuta Yamakita, Shinichi Shirakawa. "Generation of microscopic structure of solder material with desirable characteristics based on deep learning", Knowledge-Based Systems, 2022 — <1%
Publication

67 Minghui Mao, Wenwu Wang, Changheng Lu, Fengrui Jia, Xu Long. "Machine learning for board-level drop response of BGA packaging structure", Microelectronics Reliability, 2022 — <1%
Publication

68 Tzu-Chia Chen, Wang-Wang Zhu, Zi-Kun Jiao, Aleksandr Mikhailovich Petrov. "Creep–fatigue lifetime estimation of SnAgCu solder joints using an artificial neural network approach", Mechanics of Advanced Materials and Structures, 2021 — <1%
Publication

Exclude quotes	Off	Exclude matches	Off
Exclude bibliography	Off		